Monthly Notices of the ROYAL ASTRONOMICAL SOCIETY

MNRAS **518,** 2735–2745 (2023) https://doi.org/10.1093/mnras/stac3197
Advance Access publication 2022 November 07

Heating of the intracluster medium by buoyant bubbles and sound waves

Asif Iqbal,[1]★ Subhabrata Majumdar,[2] Biman B. Nath [3] and Suparna Roychowdhury [4]

[1] *Université Paris-Saclay, Université Paris Cité CEA, CNRS, AIM, F-91191 Gif-sur-Yvette, France*
[2] *Tata Institute of Fundamental Research, 1 Homi Bhabha Road, Navy Nagar, Colaba, Mumbai, Maharashtra 400005, India*
[3] *Raman Research Institute, Sadashiva Nagar, Bengaluru, Karnataka 560080, India*
[4] *Department of Physics, St. Xavier's College, Kolkata, West Bengal 700016, India*

Accepted 2022 November 3. Received 2022 November 3; in original form 2022 September 30

ABSTRACT

Active galactic nuclei (AGN) powered by the central supermassive black holes (SMBHs) play a major role in modifying the thermal properties of the intracluster medium (ICM). In this work, we implement two AGN heating models: (i) by buoyant cavities rising through stratified ICM (effervescent model) and, (ii) by viscous and conductive dissipation of sound waves (acoustic model). Our aim is to determine whether these heating models are consistent with ICM observables and if one is preferred over the other. We assume an initial entropy profile of ICM that is expected from the purely gravitational infall of the gas in the potential of the dark matter halo. We then incorporate heating, radiative cooling, and thermal conduction to study the evolution of ICM over the age of the clusters. Our results are: (i) Both the heating processes can produce comparable thermal profiles of the ICM with some tuning of relevant parameters. (ii) Thermal conduction is crucially important, even at the level of 10 per cent of the Spitzer values, in transferring the injected energy beyond the central regions, and without which the temperature/entropy profiles are unrealistically high. (iii) The required injected AGN power scales with cluster mass as $M_{\rm vir}^{1.5}$ for both models. (iv) The required AGN luminosity is comparable with the observed radio jet power, reinforcing the idea that AGNs are the dominant heating source in clusters. (v) Finally, we estimate that the fraction of the total AGN luminosity available as the AGN mechanical luminosity at $0.02\,r_{500}$ is less than 0.05 per cent.

Key words: galaxies: clusters: intracluster medium – quasars: supermassive black holes – large-scale structure of Universe.

1 INTRODUCTION

Current and future X-ray and cosmic microwave background (CMB) missions (like eROSITA, Athena, Simons Array, CMB-S4, CMB-HD, etc) have cluster cosmology and cluster physics as two of their main drivers. The synergy of cosmology and cluster gas physics, intertwined through the nature of the intracluster medium (ICM), lies at the core of realizing the science goals. The physics of the ICM is complex due to the multiple energetic physical processes, having both temporal and spatial dependence, involved in it. With the advent of the current X-ray satellites, *Chandra*, *XMM–Newton*, and *eROSITA*, it is now believed that the energetics of the ICM is regulated by heating from non-gravitational sources like active galactic nuclei (AGN) and SNe in galaxies, in addition to the heating at the accretion shock due to gravitational collapse (White & Rees 1978) and radiative cooling. One of the most important implications of these observations is that the central gas must experience some kind of heating plausibly due to the same feedback mechanism that prevents cool-cores (CCs) from establishing significant cooling flows that were predicted by earlier, low-resolution, X-ray observations (see Fabian 1994; Peterson et al 2001; Peterson et al 2006 and references therein). Establishing the source of this heating, and understanding when and how it takes place, has become a major topic of study in extra-galactic astrophysics. In addition to the cooling flow problem, another important issue that came into focus recently is the existence of an enhancement in the entropy profile within the core (<100 kpc) of the cluster (see Pratt et al. 2010, and references therein). This entropy enhancement is found to be more pronounced in non-cool-core (NCC) clusters compared to the CC clusters.

The complexities of ICM also manifest in the so-called 'cluster scaling relations'. The theory of hierarchical structure formation predicts cluster scaling relations to be self-similar (Kaiser 1986; Sereno & Ettori 2015). However, observations show departure from self-similarity; for example, the luminosity-temperature (L_x–T) relation for self-similar models predict a shallower slope ($L_x \propto T^2$) than observed ($L_x \propto T^3$) (Pratt et al. 2009). Similarly, Sunyaev–Zel'dovich (SZ) scaling relations also show similar departure (Holder 2001; Andrade-Santos et al. 2021).

Several processes have been proposed to explain the observations: pre-heating of the infalling gas due to early feedback processes in high-redshift galaxies (Babul et al. 2002), AGN feedback from quasars or radio jets (Binney & Tabor 1995; Rephaeli & Silk 1995; Nath & Roychowdhury 2002), conduction of thermal energy from the outer shock-heated regions carried by electrons (Voigt & Fabian 2004; Rasera & Chandran 2008), and gas sloshing from minor and major mergers (Fabian & Daines 1991). While the verdict is still out for early pre-heating and thermal conduction, the ability of AGN feedback to stem cooling flows, and to break self-similarity in scaling relations, has been demonstrated in several hydrodynamical simulations (Sijacki &Springel 2006; Khalatyan et al. 2008; Puchwein, Sijacki &Springel 2008; Dubois et al. 2010; Fabjan et al. 2010;

★ E-mail: asif.ahanagr@cea.fr

McCarthy et al. 2010; Teyssier et al. 2011). It seems, therefore, natural to consider such an AGN feedback mechanism as a key ingredient to account for the excess energy or entropy in the ICM. However, one still needs to understand the exact physical process that helps evolve the excess entropy with time and distance from the SMBHs powering the central AGN.

In earlier work, Iqbal et al. (2017a, b) found that the presence of non-gravitational energy per particle, related to excess entropy beyond r_{500} is almost negligible, thereby ruling out pre-heating models at a large confidence level. Subsequently, Iqbal, Nath & Majumdar (2018) showed that AGN feedback and radiative cooling are jointly responsible for the state of the ICM in the central regions, $r \lesssim 0.3\,r_{500}$. Similarly, Gaspari et al. (2014a) showed that AGN feedback can naturally regulate the thermodynamical state of ICM up to $r \approx 0.2\,r_{500}$. Given the importance of AGN feedback and radiative cooling in the inner regions and the lack of excess energy in the outer regions, it is natural to investigate the radial dependence of the feedback energetics.

There are a number of models and simulations that have been developed to explain the AGN feedback, however, their validity and applicability are mitigated by the implicit assumptions used in these models. The issue of the physical mechanism of heating remains elusive precisely for these reasons, despite the plethora of models (see, for example, Sokeri (2022) who list seven main AGN heating models). In this work, we consider two models of mechanical heating by central AGN and ignore the other heating processes. One concerns the work done by bubbles (cavities) blown by the AGN jet and carried towards the outer regions of the cluster by the pressure gradient in the ICM (Ruszkowski & Begelman 2002; Roychowdhury et al. 2004). The other model explores the possibility of heating via viscous dissipation and thermal conduction of the energy by sound waves generated by some other phenomena related to the jet (Fabian et al. 2005; Zweibel et al. 2018). These two models have been analytically worked out in detail, with heating rates written down in analytical forms, and hence can be compared to X-ray and SZ observations. It is not a priori clear whether or not the acoustic and the effervescent heating both satisfy the observations. And if they do so, it is important to determine for what values of the parameters they are valid.

In this paper, we compare these two modes of energy deposition into the ICM by AGN, combined with radiative cooling and thermal conduction, for clusters of different masses. We trace the evolution of the thermal properties of the ICM over its lifetime. Given that the ICM is not affected by feedback far from the core, we parametrize feedback models such that they affect the thermal structure of ICM up to $0.1\,r_{500}$ and $0.3\,r_{500}$. Finally, we estimate the relation between the mechanical energy injected by the AGN, and the cluster mass and compare it with scaling relations derived from the complementary observations. For simplicity, we ignore convection and cooling flows in this work. Both these effects are expected to be significant below $0.1\,r_{500}$ and we plan to consider these effects in a companion paper.

Throughout this work, we adopt a cosmology with $H_0 = 70\,\mathrm{km\ s^{-1}\ Mpc^{-1}}$, $\Omega_\mathrm{m} = 0.3$, and $\Omega_\Lambda = 0.7$. Further, $E(z)$ is the is the ratio of the Hubble constant at redshift z to its present value, H_0 and $h_{70} = H_0/70 = 1$.

2 CLUSTER MODEL

2.1 The dark matter profile

We work with the Navarro–Frenk–White (NFW) density profile (ρ_tot) (Navarro et al. 1996, 1997) of galaxy clusters given by

$$\rho_\mathrm{tot}(r) = \frac{\rho_s}{y(1+y)^2}, \tag{1}$$

where $y = r/r_\mathrm{s}$, r_s is the scale radius and ρ_s is the normalization of the density profile. The total mass profile (M_tot) of galaxy clusters can then be simply expressed as

$$M_\mathrm{tot} = 4\pi r_\mathrm{s}^3 \rho_\mathrm{s}\left[\ln(1+y) - \frac{1}{1+y}\right]. \tag{2}$$

For a given total virial mass of cluster (M_vir), the virial radius, $R_\mathrm{vir}(M_\mathrm{vir}, z)$ is found using $R_\mathrm{vir} = \left[\frac{M_\mathrm{vir}}{4\pi/3\Delta_\mathrm{c}(z)\rho_\mathrm{c}(z)}\right]^{1/3}$ (Peebles 1980), where the overdensity $\Delta_\mathrm{c}(z) = 18\pi^2 + 82(\Omega_\mathrm{m}(z) - 1) - 39\,(\Omega_\mathrm{m}(z) - 1)^2$ (Bryan & Norman 1998). The concentration parameter is related to the r_s as $c_\mathrm{vir} = R_\mathrm{vir}/r_\mathrm{s}$, where R_vir is the virial mass. Numerical simulations predict self-similar relation between c_vir and M_vir, and we adopt the expression for the concentration parameter from Duffy et al. (2008)

$$c_\mathrm{vir} = 7.85\left(\frac{M_\mathrm{vir}}{2\times10^{12}\,h^{-1}\,\mathrm{M}_\odot}\right)^{-0.081}(1+z)^{-0.71}. \tag{3}$$

The c_vir–M_vir relation from Duffy et al. (2008) has been found to be consistent with the Subaru weak lensing estimates of Okabe et al. (2010).

2.2 The fiducial ICM profile

Numerical simulations, backed by current X-ray and SZ observations, show that the ICM pressure profile follows a universal form which is well described by a generalized NFW model (Nagai et al. 2007; Arnaud et al. 2010; Planck Collaboration V 2013)

$$\frac{P_g(x)}{P_{500}} = \frac{P_0}{(c_{500}x)^\gamma[1+(c_{500}x)^\alpha]^{(\beta-\gamma)/\alpha}}, \tag{4}$$

where $x = r/r_{500}$. P_0, c_{500}, γ, α, β are the model parameters and

$$P_{500} = 1.65\times10^{-3}E(z)^{8/3} \times\left[\frac{M_{500}}{3\times10^{14}h_{70}^{-1}\,\mathrm{M}_\odot}\right]^{2/3} h_{70}^2\,\mathrm{keV\ cm^{-3}}. \tag{5}$$

P_{500} reflects the self-similar dependence with mass and redshift. Moreover, simulations have shown no significant evolution outside of the cluster core (Battaglia et al. 2012; Planelles et al. 2017), which has been also confirmed observationally (McDonald et al. 2014; Adam et al. 2015). In the present work, we consider Planelles et al. (2017) best-fitting non-radiative pressure profile ($P_0 = 6.85$, $c_{500} = 1.09$, $\gamma = 0.31$, $\alpha = 1.07$, and $\beta = 5.46$) as our baseline pressure profile. It is worth mentioning here that the Planelles et al. (2017) did not find additional mass dependence of pressure profile like in Arnaud et al. (2010). Given an initial non-radiative pressure (i.e equation (4)) and NFW model for total mass (i.e. equation 2), the density (ρ_g) profile (and hence temperature (T_g)) of the ICM can be determined using hydrostatic equation

$$\rho_\mathrm{g}(r) = \frac{r^2}{GM_\mathrm{tot}(<r)}\frac{\mathrm{d}P_\mathrm{g}}{\mathrm{d}r}. \tag{6}$$

Finally, note that the the overall conclusion of this work is independent of the choice of the initial ICM profile used, for example using non-radiative profile from Voit, Kay & Bryan (2005) would have made no significant change.

2.3 Central AGN heating

Here we discuss briefly the two models of mechanical heating by central AGN: the acoustic model and the effervescent model.

2.3.1 *Effervescent heating model*

The central AGN is responsible for inflating buoyant bubbles of relativistic plasma in the ICM in the effervescent heating model (Begelman 2001; Churazov et al. 2001; Ruszkowski & Begelman 2002; Roychowdhury et al. 2004). The time-scale for bubbles to cross the cluster, which is of the order of the free-fall time, is found to be shorter than the cooling time-scale. It is assumed that the number flux of bubbles is large such that the flux of bubble energy through the ICM approaches a steady state. This, in turn, implies that the details of the energy injection process such as the number flux of bubbles, bubble radius, filling factor and the rate of rise do not affect the average heating rate.

We assume that the relativistic gas inside the bubble does not mix with the ICM very efficiently and that bubbles push aside the X-ray emitting gas, thus excavating depressions in the ICM which should be detectable as apparent cavities in the X-ray images. Indeed, this scenario is vindicated through *Chandra* and *XMM–Newton* observations, which have seen cavities far away from the central regions of the cluster (Shin, Woo & Mulchaey 2016). In this scenario, the bubbles can expand and do $p\,\mathrm{d}V$ work on the ambient medium, as they rise in the cluster pressure gradient, thus converting the internal energy of the bubbles to thermal energy of the ICM within a pressure scale height of where it is generated. It is important to mention, although bubbles have been detected out to large radii, some 3D hydrodynamical simulations have shown a strong mixing of the bubbles with the ICM (Hillel & Soker 2020). In such cases, effervescent heating might actually be a subdominant process.

In steady state (assuming spherical symmetry) and assuming negligible mixing, the energy flux carried by the bubbles, during adiabatic bubble inflation, is given by (Begelman 2001; Roychowdhury et al. 2004)

$$F_{\rm b} \propto \frac{P_{\rm b}(r)^{(\gamma_{\rm b}-1)/\gamma_{\rm b}}}{r^2}, \tag{7}$$

where $P_{\rm b}(r)$ is the partial pressure of relativistic buoyant gas inside the bubbles at cluster radius r and the relativistic adiabatic index of buoyant gas $\gamma_{\rm b} = 4/3$. Assuming that the partial pressure inside these bubbles scales as the thermal pressure of the ICM, the volume heating rate $\epsilon_{\rm heat}\,(r)$ can be expressed as (Begelman 2001; Roychowdhury et al. 2004)

$$\begin{aligned}\epsilon_{\rm heat}(r) &\approx r^2 h(r) \nabla \cdot (\hat{\mathbf{r}} F_{\rm b}) \\ &= h(r) P_{\rm g}^{(\gamma_{\rm b}-1)/\gamma_{\rm b}} \frac{1}{r} \frac{\mathrm{d}\ln P_{\rm g}}{\mathrm{d}\ln r},\end{aligned} \tag{8}$$

where $h\,(r)$ is given by

$$h(r) = \frac{L_{\rm Eff}^{\rm inj}}{4\pi r^2}[1 - \exp(-r/r_0)]\exp(-{\rm r}/{\rm r}_{\rm cutoff})\,{\rm q}^{-1}. \tag{9}$$

In equation (9), $L_{\rm Eff}^{\rm inj}$ is the time-averaged energy injection rate, r_0 represents the transition from bubble formation region to the buoyant (effervescent) phase and $r_{\rm cutoff}$ is the outer heating cut-off radii. The term $h\,(r)$ thus takes into account the fact that the volume heating rate is maximum near the inner cut-off radius and falls off exponentially with increasing radius. In our calculations, we fix r_0 to be equal to $0.015\,r_{500}$. We note that our final results are not sensitive to the choice of r_0. The normalization factor q is defined by

$$q = \int_{r_{\rm ini}}^{r_{\rm max}} P_{\rm g}^{(\gamma_{\rm b}-1)/\gamma_{\rm b}} \frac{1}{r} \frac{\mathrm{d}\ln P_{\rm g}}{\mathrm{d}\ln r}[1 - \exp(-r/r_0)]\exp(-r/r_{\rm cutoff})\,\mathrm{d}r, \tag{10}$$

where we fix $r_{\rm max} = R_{\rm vir}$.

2.3.2 *Acoustic heating model*

In the acoustic heating model (Fabian et al. 2005; Yang & Reynolds 2016; Walker et al. 2018), the ICM is heated through the dissipation of adiabatic acoustic waves produced from the central AGN. It has been shown through hydrodynamical simulations (Sternberg & Soker 2009) that the bubbles can also excite several consecutive sound waves without the need to invoke periodic jet launching episodes. Assuming the average acoustic luminosity $L_{\rm Aco}^{\rm inj}$, injected into the ICM at r_0, the acoustic luminosity surviving a given radius r given by $L_{\rm Aco}$ will depend on the dissipation length $\ell_{\rm Aco}$ (i.e $\frac{\mathrm{d}L_{\rm Aco}}{\mathrm{d}r} = -\frac{L_{\rm Aco}}{\ell_{\rm Aco}}$) of the ICM as (Fabian et al. 2005)

$$L_{\rm Aco}(r) = L_{\rm Aco}^{\rm inj} \times \exp\left(-\int_{r_0}^{r} \frac{1}{\ell_{\rm Aco}}\,\mathrm{d}r\right). \tag{11}$$

As before, we fix r_0 to be $0.015\,r_{500}$. Assuming that heating is due to kinematic viscosity (ν) and thermal conductivity (κ), the acoustic dissipation length in the ICM can be written as (Fabian et al. 2005)

$$\ell_{\rm Aco}(r) = 697\,\frac{n_{\rm e}(T_7)^{-1}(f_{-6})^{-2}}{\left(\frac{\xi_\nu}{0.1}\right) + 11.8\left(\frac{\xi_\kappa}{0.1}\right)}\,{\rm kpc}, \tag{12}$$

where f_{-6} is the frequency of the sound wave in the units of mega year ($f_{-6} = f/(10^{-6}\,{\rm yr}^{-1})$, T_7 is the temperature of the ICM in the units of 10^7 K ($T_7 = T/10^7$), and $n_{\rm e}$ is the electron number density in cm^{-3}. ξ_ν and ξ_κ represent the viscosity and conduction fractions, respectively, of their Spitzer values in the absence of a magnetic field

$$\begin{aligned}\nu &= 1.0 \times 10^{25} T_7^{5/2} n_{\rm e}^{-1} \xi_\nu, \\ \frac{\kappa}{\rho_{\rm g} c_{\rm p}} &= 2.36 \times 10^{26} T_7^{5/2} n_{\rm e}^{-1} \xi_\kappa,\end{aligned} \tag{13}$$

where $\rho_{\rm g}$ is the gas density and $c_{\rm p}$ is the specific heat at constant pressure. The volume heating rate due to viscous and conductive dissipation is then given by

$$\epsilon_{\rm heat}(r) = \frac{L_{\rm Aco}(r)}{4\pi r^2 \ell_{\rm Aco}}. \tag{14}$$

Applying this idea to the Perseus cluster, Fabian et al. (2005) suggested energy dissipation due to frequencies in the range $f_{-6} = 0.2$–1, with the slope $\zeta = 1.8$, to balance the radiative cooling at the cluster cores. In this work, we will consider heating by sound waves with $\zeta = 1.8$ such that acoustic luminosity in a frequency interval (f, $f + \mathrm{d}f$) is given by

$$L_{\rm Aco,spec}^{\rm inj}(f) = A_{\rm norm} f^{-\zeta}, \tag{15}$$

where $A_{\rm norm}$ sets the normalization such that total acoustic injected luminosity $L_{\rm Aco}^{\rm inj}$ is given by $L_{\rm Aco}^{\rm inj} = A_{\rm norm} \int L_{\rm Aco,spec}^{\rm inj}(f)\,\mathrm{d}f$. However, we will consider different frequency ranges, depending on the radial extent of feedback, suitable for our analysis. The modified volume heating rate can then be written as

$$\epsilon_{\rm heat} = \int \frac{L_{\rm Aco,spec}^{\rm inj}(f)}{4\pi r^2 \ell_{\rm Aco}} \exp\left(-\int_{r_{\rm ini}}^{r} \frac{1}{\ell_{\rm Aco}}\,\mathrm{d}r\right)\mathrm{d}f. \tag{16}$$

Note, that the higher frequencies will produce a higher heating rate but are confined to a smaller region as opposed to lower frequencies which will produce relatively less heating but up to a larger area. The total heating is frequency averaged over the spectrum in the spectral range taken for a particular cluster.

2.4 Radiative cooling and conduction

In the case of galaxy clusters, radiative cooling is dominated by free–free emission. The emissivity per unit volume can be expressed

as

$$\epsilon_{\rm cool} = n_{\rm e}^2 \Lambda_N \frac{\mu_{\rm e}}{\mu_{\rm h}} \,{\rm erg\,s^{-1}\,cm^{-3}}, \tag{17}$$

where $\mu_h = 1.26$. We consider the cooling function '$\Lambda_{\rm N}$' from Tozzi & Norman (2001) given by

$$\Lambda_N = C_1 (kT)^{\alpha} + C_2 (kT)^{\beta} + C_3, \tag{18}$$

where $\alpha = -1.7$ and $\beta = 0.5$. The constants $C_1 = 8.6 \times 10^{-25}\,{\rm erg\,cm^3\,s^{-1}\,keV^{-\alpha}}$, $C_2 = 5.8 \times 10^{-24}\,{\rm erg\,cm^3\,s^{-1}\,keV^{-\beta}}$, and $C_3 = 6.3 \times 10^{-24}\,{\rm erg\,cm^3\,s^{-1}}$ are for metallicity of 0.3 $Z_{\odot}$.

In the presence of a thermal gradient, the heat flux due to thermal conduction is given by

$$\mathrm{F_{cond}} = -\kappa \nabla T. \tag{19}$$

One can easily see from the above equation that the Spitzer thermal conductivity ξ_{κ} has a strong dependence on the temperature structure of the ICM. Finally, the heating (or cooling) rate due to thermal conduction is given by

$$\epsilon_{\rm cond} = \frac{1}{r^2} \frac{\rm d}{{\rm d}r} \left[r^2 F_{\rm cond} \right]. \tag{20}$$

3 EVOLUTION OF THE ICM

We assume quasi-hydrostatic evolution of the ICM (Roychowdhury et al. 2004; Chaudhuri & Majumdar 2011; Nath & Majumdar 2011; Chaudhuri, Nath & Majumdar 2012) such that

$$\begin{aligned} \frac{{\rm d}r}{{\rm d}M_{\rm g}} &= \frac{1}{4\pi r^2 \rho_{\rm g}(r)} = \frac{1}{4\pi r^2} \left(\frac{\sigma_{\rm g}(r)}{P_{\rm g}(r)} \right)^{1/\gamma}, \\ \frac{{\rm d}P_{\rm g}}{{\rm d}M_{\rm g}} &= \frac{G M_{\rm tot}(<r)}{4\pi r^4}, \end{aligned} \tag{21}$$

where $\sigma_{\rm g}(r) = P_{\rm g}(r)/\rho_{\rm g}(r)^{\gamma}$ is called the entropy index which is related to entropy of a gas ($K_{\rm g}$) as $K_{\rm g}(r) = \mu_{\rm g}\,\mu_{\rm e}^{2/3}\,m_{\rm p}^{5/3}\sigma_{\rm g}(r)$, and $M_g(r)$ is the gas mass enclosed up to the radius r. In the above equation $\gamma = 5/3$ is the adiabatic index, $m_{\rm p}$ is the mass of the proton, $\mu_{\rm g} = 0.59$ and $\mu_{\rm e} = 1.14$.

The ICM properties are calculated by solving equation (21) in time steps of Δt after incorporating heating, radiative cooling, and conduction. The entropy index at a given radius changes by amount

$$\Delta\sigma_{\rm g}(r) = \frac{2}{3} \frac{\sigma_{\rm g}(r)}{P_{\rm g}(r)} \left[\epsilon_{\rm heat}(r) - \epsilon_{\rm cool}(r) - \epsilon_{\rm cond}(r) \right] \Delta t. \tag{22}$$

In order to consider the redistribution of gas on account of heating and cooling, one much update the entropy index in each time-step with respect to the same gas mass shells as

$$\sigma_{\rm g}(M_{\rm g}) \rightarrow \sigma_{\rm g}(M_{\rm g}) + \Delta\sigma_{\rm g}(M_{\rm g}). \tag{23}$$

The boundary condition for equation (21) is updated such that pressure at the gas mass shell initially at virial radius, is always equal to its initial pressure. Since, we heat the ICM up to the maximum radius of 0.3 r_{500}, we see that the boundary condition has no effect on the derived pressure profile in the inner regions where the impact of feedback is signification. The second boundary condition assumes $M_{\rm g} \approx 0$ at $r \approx 0$.

For numerical stability, the conduction term is integrated using time steps that satisfy the Courant condition (Ruszkowski & Begelman 2002)

$$\Delta t_{\rm cond} \leq 0.5 \frac{(\Delta r)^2 n\, k_{\rm b}}{\xi_{\kappa}(\gamma - 1)}. \tag{24}$$

Using the above time steps, we need to evolve the cluster profiles for the age of the cluster. We define the cluster formation epoch as the time when the cluster has a mass greater than $\frac{3}{4} M_{\rm vir}$ for the first time. This assumption is motivated by the results of the numerical simulations, which show that gravitational potential does not change much after the cluster assembles its $\frac{3}{4}$ of its total mass Navarro et al. (1997). Using this definition for the epoch of cluster formation, Nath (2004) found a convenient fit for the cluster age ($t_{\rm age}$), for a cluster, observed at a redshift of z

$$t_{\rm age} = 2.5 \times 10^9 {\rm yr}\,(1+z)^{-2.6} \left(\frac{M_{\rm vir}}{10^{14}\,{\rm M_{\odot}}} \right)^{-0.09}. \tag{25}$$

We consider the AGN duty cycle, which is defined as the fraction of time the AGN heating is active (or ICM possesses radio bubbles), to be 50 per cent. This value is the lower limit of the duty cycle as found by Dunn & Fabian (2006), Bîrzan et al. (2012). The cooling and conduction terms, on the other hand, are kept always on throughout the cluster age.

For our analysis, we will assume $\xi_{\kappa} = \xi_{\nu} = 0.1$ as our fiducial conductivity and viscosity fractions. In the next section, we will see the importance of conduction in distributing the heating of the ICM. In contrast, the viscosity fraction, ξ_{ν}, has a negligible impact on the heating profile since the dissipation length is highly dependent on ξ_{κ} through equation (12).

The degree and extent of heating of ICM in the effervescent model are effectively controlled by two parameters $L_{\rm Eff}^{\rm inj}$ and $r_{\rm cutoff}$, while the corresponding two parameters for the acoustic model are: $L_{\rm Aco}^{\rm inj}$ and f_{-6}. In both cases, the $L_{\rm Eff}^{\rm inj}$ or the $L_{\rm Aco}^{\rm inj}$ controls the amplitude, i.e the overall heating, and should be linked to the energy spewed out by the central supermassive back hole (SMBH). Indeed, as we show later, the injected energy has a simple scaling relation with the mass of the black hole (related together by the underlying $M_{\rm BH}$–$M_{\rm halo}$ relation. The parameters $r_{\rm cutoff}$ and f_{-6} control the overall shape of the heating profiles, i.e it controls the radii beyond which heating exponentially/sharply falls. For the effervescent model, it is natural to assume heating cut-off parameter $r_{\rm cutoff}$ to be also 0.1 r_{500} and 0.3 r_{500} since both observations (Iqbal et al. 2017b), and simulations (Gaspari et al. 2014a) shows no significant non-gravitational heating beyond (0.1–0.3) r_{500}. Similarly, for the acoustic model, the radial range of the feedback can be suitably controlled by limiting the frequency spectrum. Since the perturbation by the sound wave depends on the wavelength, which is inversely proportional to the frequency, one can choose a minimum frequency such that the length-scale matches 0.1 r_{500} and 0.3 r_{500} beyond which there should not be excess heating. In practice, the maximum wavelength needs to be less than 0.1 r_{500} or 0.3 $r_{500,}$ since conduction helps in propagating the heat further. We fix frequency range to be $f_{-6} = 0.05$–0.20 and $f_{-6} = 0.01$–0.20 such that the extent of feedback is only up to 0.1 r_{500} and 0.3 r_{500}, respectively. The choice of increasing the upper cut-off in frequency leading to wavelengths less than the injection length-scale has a negligible effect on the results. Once, $r_{\rm cutoff}$ or f_{-6} is fixed to achieve, the radial dependence one has to find a suitable overall amplitude $L_{\rm Eff}^{\rm inj}$ ($L_{\rm Aco}^{\rm inj}$) such that there is excess energy (entropy) up to a given radius. Finally, we note that heating due to a single frequency of $f_{-6} = 0.01$ or less is not favored by X-ray observations. Such frequencies correspond to density perturbations on length-scales of $\geq$100 kpc, for sound speed of 1000 km s^{-1} (Walker et al. 2018), which would have been easily observed by *Chandra* or *XMM–Newton* if present. However, if the acoustic heating is produced by the waves with a frequency spectrum, it would be difficult to separate out different perturbation modes through current X-ray observations.

4 RESULTS

4.1 Initial heating and cooling profiles

We start by comparing the initial heating and cooling profiles in the absence of any evolution of the ICM. Since the injected initial luminosity depends on the central black hole physics, and is hence independent of the feedback models, we assume the same mechanical luminosity for a given cluster mass in both of the heating models. This is shown in Fig. 1, where the left-hand panel shows the cooling rate versus heating rate in the ICM for the effervescent model using initial Planelles et al. (2017) profile for three cluster masses: $2 \times 10^{14}\,M_{\odot}$ (upper panel), $6 \times 10^{14}\,M_{\odot}$ (middle panel), and $2 \times 10^{15}\,M_{\odot}$ (bottom panel) at redshift $z = 0$. The parameters of the heating model are roughly chosen such that heating not only balances the cooling but also produces excess energy in the cluster cores. One can see that the heating rate with $r_{\rm cutoff} = 0.3\,r_{500}$ (blue line) and $r_{\rm cutoff} = 0.1\,r_{500}$ (red line) produces excess energy in the cluster cores for all the three cluster masses. Increasing $L^{\rm inj}_{\rm Eff}$ further will only increase the normalization of the heating profiles. As expected, a higher amount of energy feedback is required for massive clusters.

For the acoustic case, the right-hand panel in Fig. 1 shows the heating profiles for the same three cluster masses by considering spectrum having $\zeta = 1.8$ in the frequency ranges $f_{-6} = 0.01$–0.20 (solid blue line) and $f_{-6} = 0.05$–0.20 (solid red line), and with $\xi_\kappa = \xi_\nu = 0.1$. For comparison, we also show the heating profiles for two single frequencies, $f_{-6} = 0.01$ (dashed blue line) and $f_{-6} = 0.05$ (dashed red line). We find that for a spectrum of frequencies, the heating rate is dominated by the lowest frequency (i.e $f_{-6} = 0.01$ or 0.05). We note that the effective radial range of heating can be reduced not only by increasing the frequency but by also increasing the conductivity fraction ξ_κ. As in the effervescent case, changing the magnitude of acoustic luminosity only changes the normalization of the heating profiles. As can be seen in the figure, the heating profiles having frequency spectrum of $\zeta = 1.8$ with frequencies $f_{-6} = 0.01$–0.20 (or $f_{-6} = 0.05$–0.20) produces more realistically decreasing heating profiles, unlike in single frequency case, say, with $f_{-6} = 0.01$, where the heating profile is flatter in the inner region and then suddenly drops. This is easy to understand since a range of frequencies affects a range of length-scales with an average contribution to all the scales till it reaches the lowest frequency (or highest wavelength), after which the heating falls off; on the other hand, a single frequency only has one dissipation length, and the heating drastically falls beyond that radius. Therefore, we will only consider the acoustic model having a frequency spectrum in the rest of our calculations. Next, we turn our attention to the evolution of thermodynamical profiles as a response to heating, cooling, and conduction.

4.2 Evolution of the ICM with effervescent heating

Fig. 2 shows the evolution of pressure (top), entropy (middle), and temperature (bottom) for the $6 \times 10^{14}\,M_{\odot}$ cluster by considering effervescent model with $L^{\rm inj}_{\rm Eff} = 2.5 \times 10^{45}$ ergs s^{-1}, $r_{\rm cutoff} = 0.3\,r_{500}$ (left-hand panel), $L^{\rm inj}_{\rm Eff} = 4.5 \times 10^{44}$ ergs s^{-1}, and $r_{\rm cutoff} = 0.1\,r_{500}$ (right-hand panel) for the 'entire' cluster radial range, i.e (0.02–3) r_{500}. The evolution also includes the cooling and conduction ($\xi_\kappa = 0.1$). The values of $L^{\rm inj}_{\rm Eff}$ are chosen so as to produce excess energy up to $0.3\,r_{500}$ (left-hand panel) and $0.1\,r_{500}$ (right-hand panel). The profiles are evolved for the time period of $t_{\rm age} = 2.2 \times 10^9$ yr with the AGN heating switched off at half the time interval. Cooling and conduction, on the other hand, are always present throughout the age of the cluster. The time steps used to evolve the ICM is taken to be $\approx 10^4$–10^5 yr. However, in the figure, the profiles are plotted after each $\approx 1.3 \times 10^8$ yr (thin dashed lines). The initial profiles prior to heating are represented by thick solid blue lines in all the subpanels. Similarly, the final profiles at the end of $t_{\rm age}$ are shown by thick solid black lines. As the heating is turned on, the pressure profiles start to decrease until the heating is stopped (at $0.5\,t_{\rm age}$), after which profiles start to rise back slowly. This is due to the fact that the gas is pushed out due to the central heating, which later falls back. We see that the pressure profiles during the evolution are always within the Planck Collaboration V (2013) observed dispersion. The entropy and temperature profiles, as expected, show a reverse trend. They initially increase and then decrease after the heating is switched off. The fractional difference between the initial and final profiles is also shown in Fig. 2. One can see that the fractional difference can be more than 50 per cent near the centre and has a very strong central radial dependence. We can also see that the fractional difference profiles becomes zero at $\sim 0.1\,r_{500}$ and $\sim 0.3\,r_{500}$, as expected.

4.3 Evolution of the ICM with acoustic heating

Similarly, the evolution of thermal profiles with acoustic heating, cooling, and conduction is shown in Fig. 3. We assume a frequency spectrum with $\zeta = 1.8$ and $\xi_\kappa = \xi_\nu = 0.1$. We choose the same values of mechanical luminosity as that in effervescent heating. We see that an acoustic luminosity of $L^{\rm inj}_{\rm Aco} = 2.5 \times 10^{45}$ ergs s^{-1} in the frequency range of $f_{-6} = 0.01$–0.20, and an acoustic luminosity of $L^{\rm inj}_{\rm Aco} = 4.5 \times 10^{44}$ ergs s^{-1} in the frequency range of $f_{-6} = 0.05$–0.20 could produces excess energy up to $0.3\,r_{500}$ and $0.1\,r_{500}$, respectively. Our results show that the optimal frequency range should be smaller than the frequency range of $f_{-6} = 0.2$–1, as predicted by Fabian et al. (2005) so as to produce the feedback up to $0.1\,r_{500}$ or $0.3\,r_{500}$. Similar to the effervescent case, here also, the pressure (entropy) profile is pushed up (down) in the inner regions as the ICM is heated and then rises (falls) after the heating is shut off. Moreover, pressure profiles during the evolution also lie within the observed Planck Collaboration V (2013) dispersion. Similarly, the fractional change (also shown in Fig. 3) can be more than 50 per cent near the centre in the acoustic heating. One finds that in the case of acoustic heating, one gets sharp discontinuities around 0.04–$0.05\,r_{500}$ in the entropy and temperature profiles as soon as the cluster is heated which then moves forward with time evolution. However, as soon as heating is turned off, due to conduction, one recovers smooth profiles at the end of evolution. It is also likely that acoustic heating due to frequencies $f_{-6} < 0.01$ and $f_{-6} > 0.20$ are likely to be suppressed – the former range of frequencies would require a relatively large value of injected luminosity to balance the cooling, while the later range of frequencies would inject energy only into the very central region (producing very high entropy/temperature).

4.4 Importance of conductivity

Currently, there are no observational constraints about the level of conduction and convection, be it at a local or global scale. They could be significant or they may be totally suppressed. We find that for both heating models, conductivity is crucial to produce realistic thermal profiles. In the Fig. 4, we show the final pressure and entropy profiles for a $6 \times 10^{14}\,M_{\odot}$ cluster when conductivity is neglected (i.e, $\xi_\kappa = 0$) for both the heating models for same values of mechanical energy as used before. As can be seen, ignoring conductivity results in the negative gradient in entropy profiles near the cluster centre, which correspond to the unreasonable central

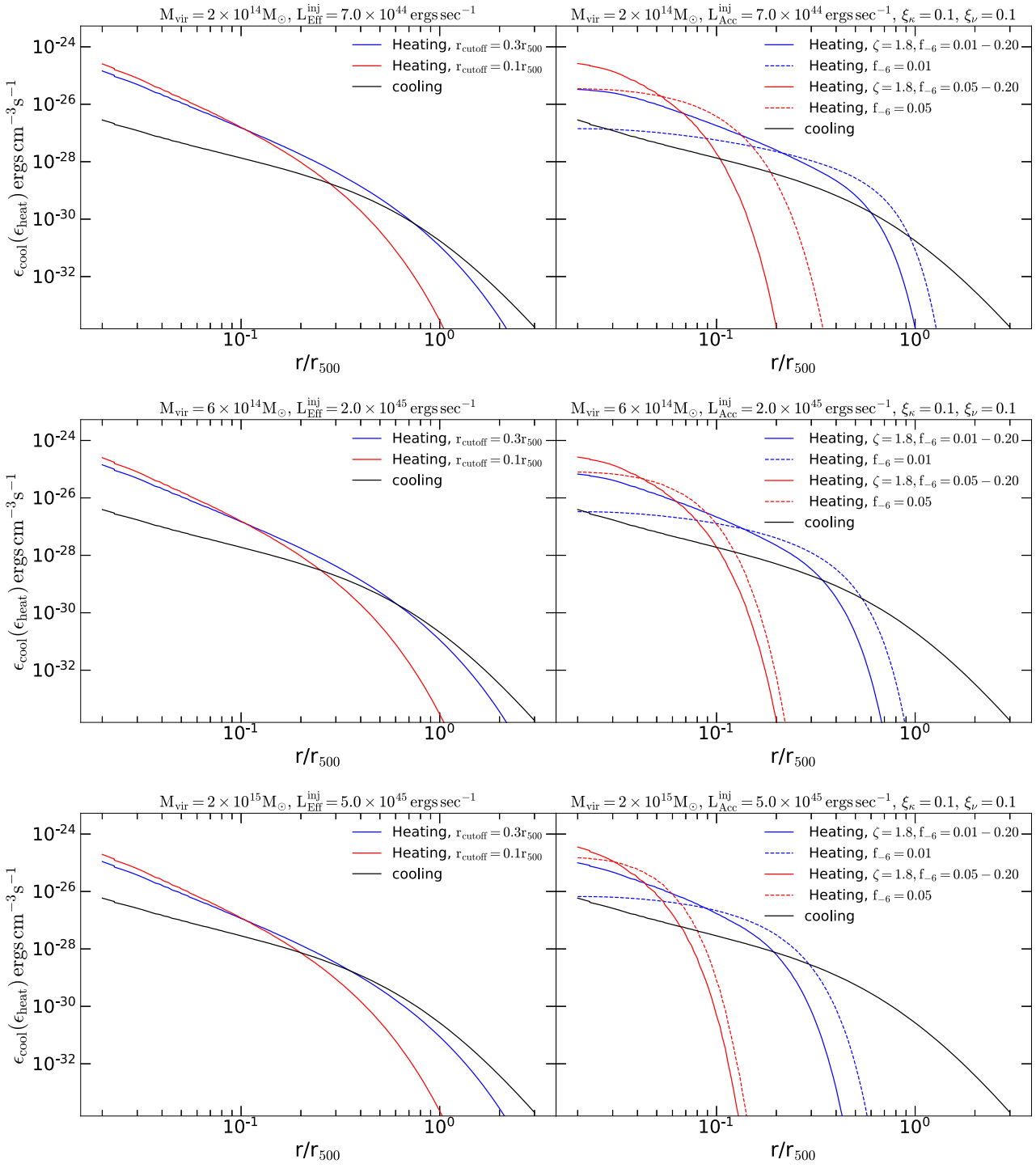

Figure 1. Comparing cooling and heating rate for effervescent and acoustic models for three different cluster masses. Left-hand panels: Initial cooling rate (black line) versus heating rate (blue and red lines) in effervescent case for $2 \times 10^{14}\,M_\odot$ (top), $6 \times 10^{14}\,M_\odot$ (middle), and $2 \times 10^{15}\,M_\odot$ (bottom) clusters at $z = 0$. Right-hand panels: Initial cooling rate (black line) versus heating rate with $\xi_\kappa = 0.1$ and $\xi_\nu = 0.1$ (blue and red lines) in acoustic case for $2 \times 10^{14}\,M_\odot$ (top), $6 \times 10^{14}\,M_\odot$, (middle) and $2 \times 10^{15}\,M_\odot$ (bottom) clusters at $z = 0$. Note that in case of acoustic heating, solid lines are obtained by assuming a frequency spectrum of $\zeta = 1.8$ and frequency range of $f_{-6} = 0.01$–0.20 (solid blue line), $f_{-6} = 0.05$–0.20 (solid red line), while as dashed lines represent heating profiles for single frequency of $f_6 = 0.01$ (dashed blue line) and $f_{-6} = 0.05$ (dashed red line).

temperature (30–100 keV); however, pressure remains less affected. The negative entropy gradient will set-up a convection, which will also help in making entropy flat. This suggests that convection (turbulence) could be a critical process, especially if conduction is absent. However, modelling convection will also require assumptions regarding mixing length and the conclusions may be dependent on it. We plan to have a companion paper, where we will have a detailed study importance of convection along with conduction. We see that heating becomes more centrally peaked in the acoustic model compared to the effervescent heating, and it becomes difficult

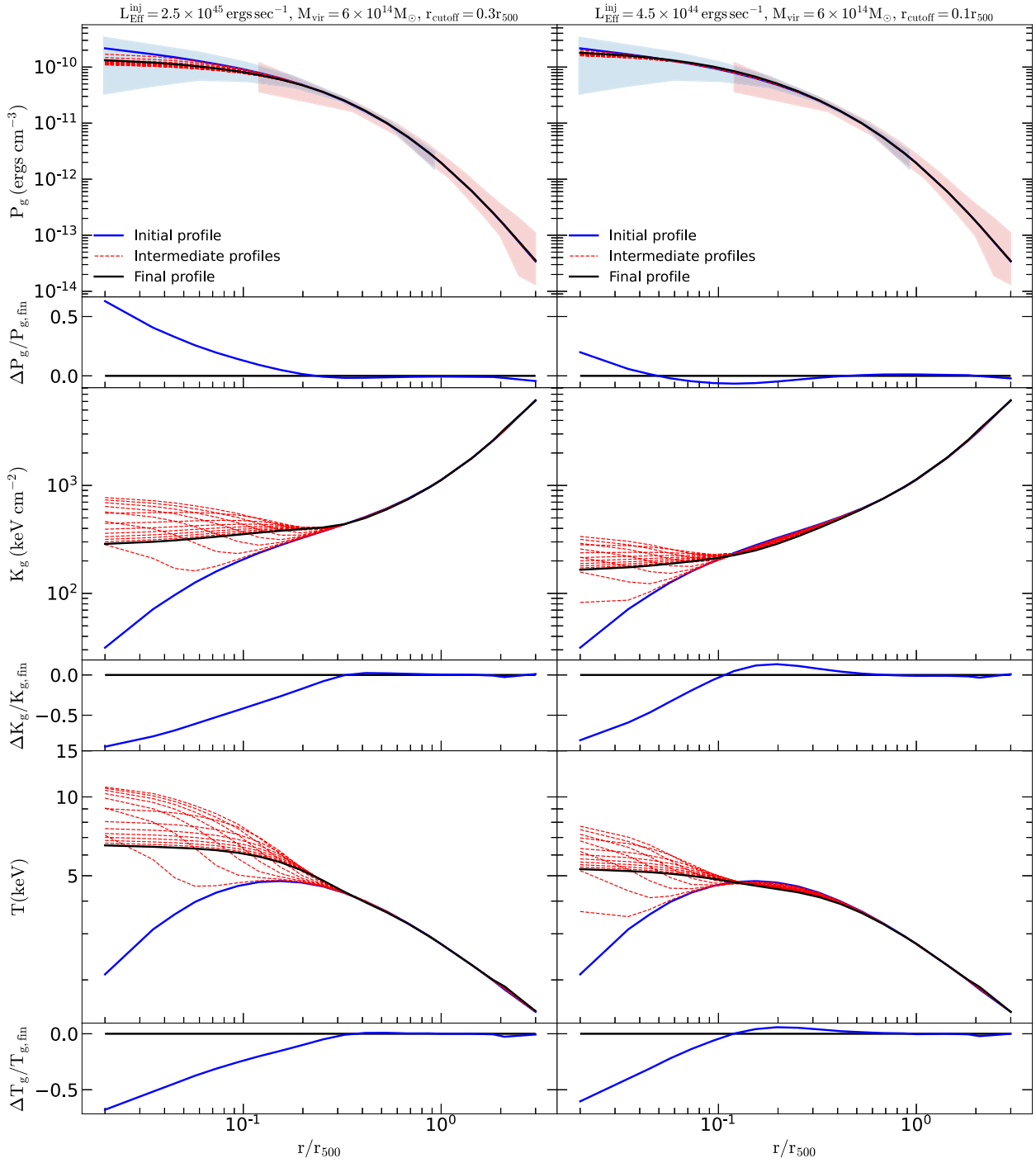

Figure 2. ICM thermodynamics for the effervescent model. Evolution of pressure (top), entropy (middle), and temperature (bottom) profiles as a function of radius in effervescent heating for a cluster of mass $6 \times 10^{14}\,M_\odot$ at $z = 0$ with $r_{cutoff} = 0.3\,r_{500}$ (left-hand panel) and $r_{cutoff} = 0.1\,r_{500}$ (right-hand panel), with cooling and conduction ($\xi_\kappa = 0.1$) included. The evolution of the profiles is shown at intervals of 13×10^8 yr with thin red dashed lines. The total evolution time is $t_{age} = 2.2 \times 10^9$ yr and heating is turned on during the first half of the evolution. Cooling and conduction are present throughout the evolution. The pressure (entropy) is seen to fall (rise) as the gas is heated and then rise (fall) after the heating is switched off. Initial and final states correspond to thick solid blue and black lines, respectively. The blue and red shaded regions are the dispersion of the stacked *XMM–Newton* and Planck pressure profiles of 62 clusters form Planck Collaboration V (2013) (their figure 4). For each panel, we also show the fractional change between the initial and final profiles ($P_{g,fin}$, $K_{g,fin}$, $T_{g,fin}$).

to achieve feedback beyond $0.05\,r_{500}$. In general, the impact of conduction lies in the fact that it tries to make the ICM isothermal by transporting the large amount of energy injected near the centre to the outer region, which results in the entropy/temperature flattening. This can be seen in Figs 2 (effervescent model) and 3 (acoustic model), where the final temperature profiles become more or less flat in the inner regions with $\xi_\kappa = 0.1$. In the case of effervescent heating, for a given L_{Eff}^{inj}, higher values of the conductivity fraction will try to make the gas temperature uniform more efficiently without changing the final profiles significantly. In particular, with conduction, we can have

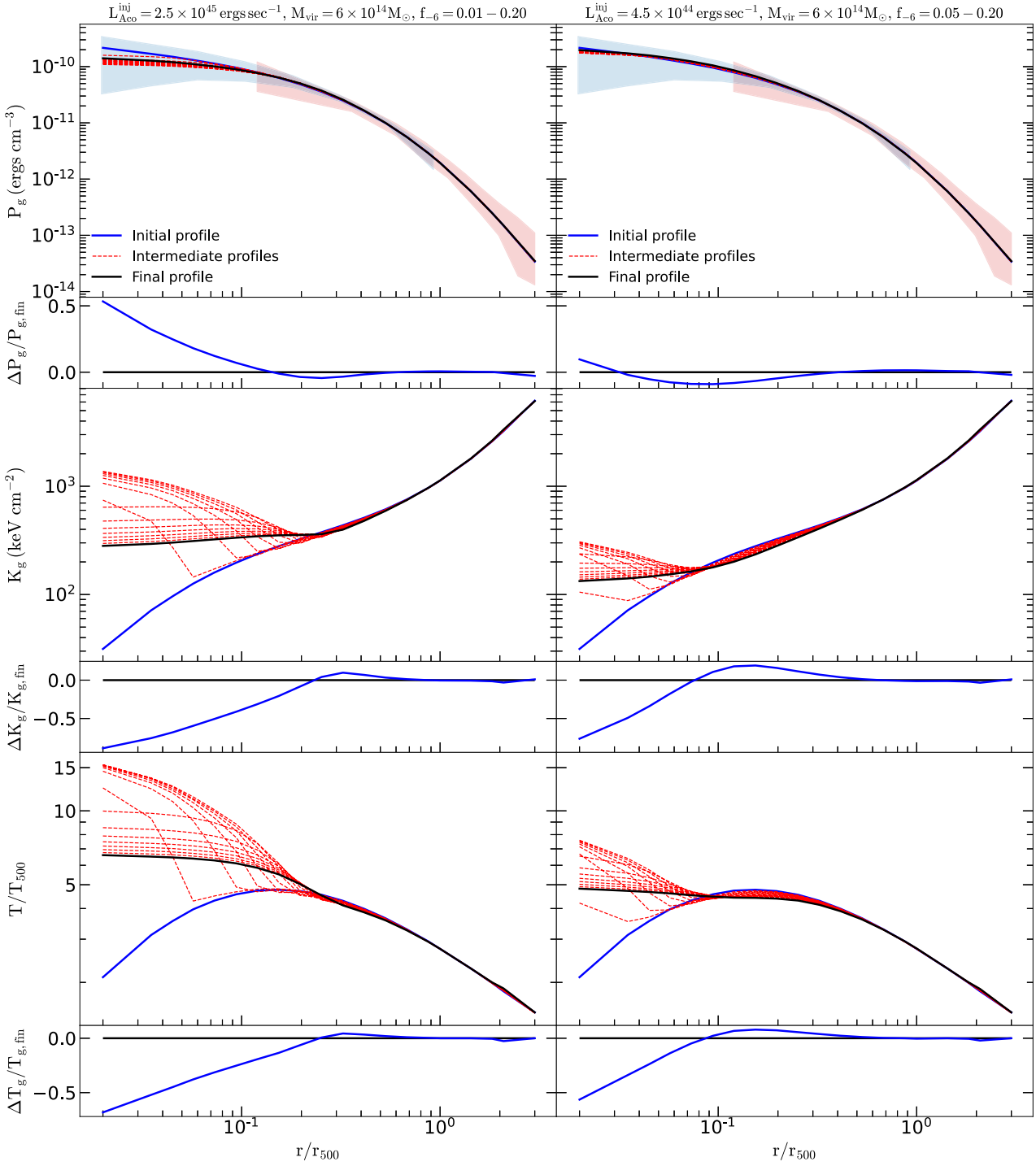

Figure 3. ICM thermodynamics for the acoustic model. Evolution of pressure (top), entropy (middle), and temperature (bottom) profiles as a function of radius in acoustic heating for a cluster of mass 6×10^{14} M$_\odot$ at $z = 0$ with spectrum $\zeta = 1.8$ and $f_{-6} = 0.01$–0.20 (left-hand panel) and $f_{-6} = 0.05$–0.20 (right-hand panel). The evolution also includes cooling and conduction with $\xi_\kappa = 0.1$ and $\xi_\nu = 0.1$. The evolution of the profiles is shown at intervals of 13×10^8 yr with thin red dashed lines. The total evolution time is $t_{age} = 2.2 \times 10^9$ yr and heating is turned on during the first half of the evolution. Cooling and conduction are present throughout the evolution. The pressure (entropy) is seen to fall (rise) as the gas is heated and then rise (fall) after the heating is switched off. Initial and final states correspond to thick solid blue and black lines, respectively. The blue and red shaded regions are the dispersion of the stacked *XMM–Newton* and Planck pressure profiles of 62 clusters form Planck Collaboration V (2013) (their figure 4). For each panel, we also show the fractional change between the initial and final profiles ($P_{g,fin}$, $K_{g,fin}$, $T_{g,fin}$).

energy feedback reach to $0.3\,r_{500}$ even with a lower $r_{cutoff} = 0.1\,r_{500}$, and end up with similar final profiles as those obtained obtained with $L^{inj}_{Eff} = 2.5 \times 10^{45}$ and $r_{cutoff} = 0.3\,r_{500}$. Its impact is more complex in the acoustic model where the heating also depends on the value of ξ_κ. One finds that ignoring conductivity in the acoustic model decreases the overall amplit ude of the heating profiles; however, the effective heating profile extends to a larger radius, and one requires a relatively larger value of L^{inj}_{Aco} to balance the cooling near the centre.

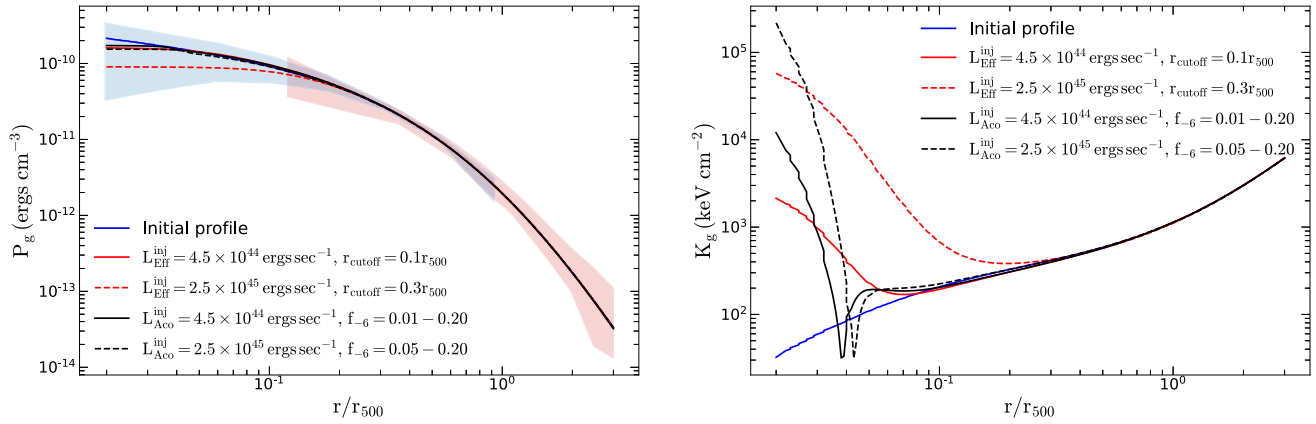

Figure 4. Final pressure (left-hand panel) and entropy (right-hand panel) for effervescent and acoustic heating without considering conduction ($\xi_\kappa = 0$) for 6×10^{14} M$_\odot$ cluster mass.

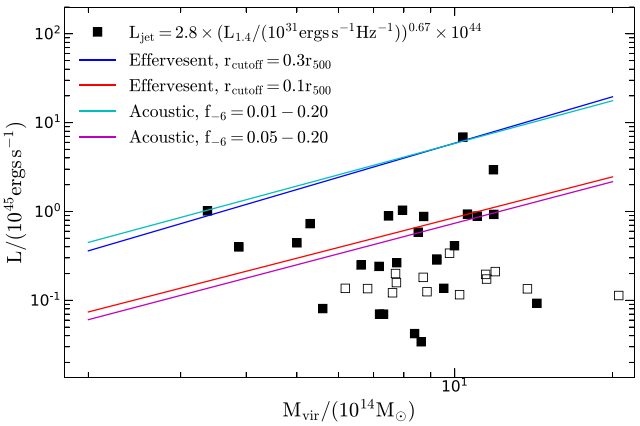

Figure 5. Relation between average injected luminosity and the cluster mass for different cases. Blue and red lines are the best-fitting relation for the effervescent heating for $r_{cutoff} = 0.3\, r_{500}$ and $r_{cutoff} = 0.1\, r_{500}$, respectively. Cyan and magenta lines are the best-fitting relation for the acoustic heating for frequency spectrum of $\zeta = 1.8$ with $f_{-6} = 0.01$–0.20 and $f_{-6} = 0.05$–0.20, respectively. Also shown is the expected mechanical jet power L_{jet} (squares) from $L_{1.4}$ measurements of Kale et al. (2015), using Godfrey & Shabala (2013) L_{jet}–$L_{1.4}$ relation for cluster of masses $\geq 10^{14}$ M$_\odot$. Open squares are based on radio upper limits.

For a given L^{inj}_{Aco}, as we increase the ξ_κ from our fiducial value of 0.1, the heating rate becomes more centrally peaked but so does the conduction from the central region to the outer region. This makes the final temperature profile more or less isothermal in the inner region. Moreover, we find that due to the very high central heating arising with frequency ranges $f_{-6} > 0.01$, it is not possible to have reasonable feedback profiles up to $0.3\, r_{500}$ (especially for the high-mass clusters) even though final profiles are isothermal in the inner region.

4.5 Comparison with the observations

Given that we can calculate the AGN feedback needed to balance cooling up to a certain radius for both scenarios of heating, we can estimate the mass dependence of the central injected energy. Here, we study the evolution of ICM properties of the galaxy clusters in the range 2×10^{14}–2×10^{15} M$_\odot$. The Fig. 5 shows the derived scaling relation between the injected effervescent (acoustic) luminosity with the total mass of the cluster such that one gets excess energy up to $0.1\, r_{500}$ or $0.3\, r_{500}$. For the effervescent heating and assuming $\xi_\kappa = 0.1$ we get

$$\log\left(\frac{L^{inj}_{Eff}}{10^{45}\text{ ergs sec}^{-1}}\right) = -0.96 + 1.73 \log\left(\frac{M_{vir}}{10^{14}\,M_\odot}\right) \quad \text{for } r_{cutoff} = 0.3 r_{500},$$

$$\log\left(\frac{L^{inj}_{Eff}}{10^{45}\text{ ergs sec}^{-1}}\right) = -1.58 + 1.52 \log\left(\frac{M_{vir}}{10^{14}\,M_\odot}\right) \quad \text{for } r_{cutoff} = 0.1 r_{500}, \tag{26}$$

Similarly for the acoustic heating and assuming $\xi_\kappa = \xi_\nu = 0.1$, we get

$$\log\left(\frac{L^{inj}_{Aco}}{10^{45}\text{ ergs sec}^{-1}}\right) = -0.82 + 1.59 \log\left(\frac{M_{vir}}{10^{14}\,M_\odot}\right) \quad \text{for } f_{-6} = 0.01\text{–}0.20,$$

$$\log\left(\frac{L^{inj}_{Aco}}{10^{45}\text{ ergs sec}^{-1}}\right) = -1.68 + 1.55 \log\left(\frac{M_{vir}}{10^{14}\,M_\odot}\right) \quad \text{for } f_{-6} = 0.05\text{–}0.20. \tag{27}$$

Interestingly, as can be seen in the figure (and the above relations), both heating models give a similar scaling for feedback. One finds the same slope, L^{inj}_{Eff} (or L^{inj}_{Aco}) $\propto M_{vir}^{\sim 1.5}$ when heating and cooling are balanced up to $0.1\, r_{500}$; however, the slope for the effervescent model scaling relation is slightly steeper than acoustic model when we consider energy balance up to a higher radius of $0.3\, r_{500}$. Also plotted, in the same figure is the estimated mechanical jet power, L_{jet}, using the BCG radio luminosity measurements at 1.4 GHz, $L_{1.4}$, for the cluster sample used in Iqbal et al. (2018)[1] (their table 1) by considering Godfrey & Shabala (2013) L_{jet}–$L_{1.4}$ relation for FRII galaxies and using a spectral index of 0.6

$$L_{jet} = 2.8 \times \left(\frac{L_{1.4}}{10^{31}\text{ ergs s}^{-1}\text{Hz}^{-1}}\right)^{0.67} \times 10^{44}\text{ ergs s}^{-1}. \tag{28}$$

We see that the feedback up to $0.3\, r_{500}$ represents the upper limit of the observed mechanical luminosity and that most of the data centres around $0.1\, r_{500}$. Note that there can be other fainter radio sources that have evaded detection but which still contribute to the heating of the ICM.

[1] M_{vir} is assumed to be $1.25 \times M_{500}$.

Assuming that the scaling between the central black hole mass and the virial mass of a galaxy halo, $M_{\rm BH} \approx 10^{9.5}(M_{\rm vir}/(10^{14}\,{\rm M}_\odot))^{1.5}$, as given by Bandara, Crampton & Simard (2009) holds for cluster scales, one finds that that AGN mechanical luminosity can be approximated as $L_{\rm inj} \approx 10^{44}\,{\rm ergs\ s^{-1}}\ M_{\rm BH}/(10^{9.5}\,{\rm M}_\odot)$. Comparing this with the Eddington luminosity of the central SMBH, $L_{\rm Edd} \approx 10^{47.5}\,{\rm ergs\,s^{-1}} M_{\rm BH}/(10^{9.5}\,{\rm M}_\odot)$, one can see that the fraction of the total luminosity available as the AGN mechanical luminosity at $0.02\,r_{500}$ is given by $\epsilon_{\rm inj} = L_{\rm inj}/L_{\rm Edd} \approx 10^{-3.5}$. This falls at the lower end of the range of values used in AGN feedback simulations for the super-Eddington accretion in order to explain the rapid assembly of $10^9\,{\rm M}_\odot$ SMBHs in the first billion years of the Universe (Massonneau et al. 2022).

5 DISCUSSION AND CONCLUSIONS

It is interesting to compare our results with the constraints on the total injected energy from the central AGN estimated for effervescent heating by Roychowdhury, Ruszkowski & Nath (2005). They showed that if the heating time, $t_{\rm heat}$, lies between 5×10^8 to 5×10^9 yr, the average jet luminosity, $L^{\rm inj}$, would vary between 5×10^{44}–2×10^{45} erg sec^{-1} for cluster masses ranging from 4×10^{13}–$10^{15}\,{\rm M}_\odot$. This total heating time might include short multiple episodes of the central black hole, with bubbles consisting of relativistic plasma from earlier active phases, being spread out all through the cluster atmosphere. The authors concluded that it was possible to fit the excess entropy requirements for clusters of different masses with only one pair of $L^{\rm inj}$ and $t_{\rm heat}$. They found the total energy injected into the ICM (and hence injected luminosity) to be proportional to $M_{\rm vir}^{1.5}$, which agrees perfectly with our estimates. Moreover, they also estimated that this scaling is consistent with a relation between the supermassive black hole mass ($M_{\rm bh}$) in the central AGN and the cluster mass, $M_{\rm bh} \sim 10^{-5} M_{\rm vir}$, if the efficiency of conversion of energy by the accreting black hole is ∼0.25. This scaling is reminiscent of the relation between black hole mass and galaxy mass (Bandara et al. 2009).

It is worthwhile to point out that the robustness of these heating models rests upon the fact that the injected luminosity from the central AGN, be it effervescent or acoustic heating or a combination of both, lies in a similar range as demonstrated in this work. It is only natural to propose that both effervescent and acoustic heating are occurring in tandem with thermal conduction playing an important role in distributing the heat to the outer regions of the cluster atmosphere. It is also important to note that other heating processes can be more important than the two models discussed here (for example, see Hillel & Soker (2020)), and that the conclusions of the present paper hold only if we ignore the other heating mechanisms. Moreover, we emphasize that both heating models considered in this work have several parameters, like $L^{\rm inj}_{\rm Eff}$ ($L^{\rm inj}_{\rm Aco}$), which is assumed constant, duration of the heating, and we assume the spherical model of heating.

Currently, our approach does not account for the observed diversity between CC and NCC clusters. In particular, we find that our heating model is not able to reproduce high densities and low entropy in the inner regions as found in CC clusters. Therefore, it still remains to explain the wide variety of observed ICM properties, especially, the CC/NCC dichotomy observed in the population of galaxy clusters. Dubois et al. (2011) found that the interaction between an AGN jet and the ICM gas that regulates the growth of the AGN's black hole, can naturally produce CC clusters if the contribution of metals is neglected. However, as soon as metals are allowed to contribute to the radiative cooling, only the NCC solution is produced. Similarly, it has also been argued that anisotropic thermal conduction (Barnes et al. 2019) or artificial conduction (Rasia et al. 2015) which enhances the mixing of gas might naturally explain the formation of CC and NCC clusters. An immediate extension of the present work is to include cooling flows in the very central region since that would help us to produce CCs if the mass accretion rate is high enough (Nath 2003). Additionally, one can also include convection in the evolution which will also help to make the gas isothermal. Moreover, the derived feedback profiles can be compared with precise multi-wavelength observations of galaxy clusters in the Cluster HEritage project (CHEX-MATE Collaboration 2021), which will allow us to probe the extent of AGN feedback in the galaxy clusters.

The main focus of this work is to quantitatively compare effervescent and acoustic models of heating in the ICM. We study the evolution of ICM thermal profiles with these two models of AGN heating along with conduction and cooling in the clusters of mass range of 2×10^{14}–$2 \times 10^{15}\,{\rm M}_\odot$ at redshift, $z = 0$ so as to produce excess energy up to $0.1\,r_{500}$ or $0.3\,r_{500}$. The heating can be controlled by tuning relevant parameters of the heating models. For effervescent heating, the relevant parameter is the outer radial cut-off of the heating, and for acoustic heating, it is the frequency of the plasma waves. We find that for acoustic heating to work in the range 0.1–0.3 r_{500}, the optimal frequencies should lie in the range of $f_{-6} = 0.01$–0.20. We find that one additionally requires conduction which significantly influences the properties of the ICM. As a result of the conduction, injected heat flows from the innermost regions of the cluster to the outer regions thus erasing strong temperature gradients. We also estimate the relation between the injected luminosity required to match the observations and the cluster mass. We find that both effervescent and acoustic produce the same scaling relations thus making it difficult to disentangle the heating models with the X-ray and SZ observations. We find injected luminosity scales with cluster mass as $M_{\rm vir}^{\sim 1.5}$ for both effervescent and acoustic heating. Moreover, the inferred correlation is consistent with the observed mechanical jet power and radio luminosity relation, reinforcing the idea that AGNs provide the most dominant heating in the ICM.

To conclude, It has been shown that the power spectrum of density/pressure fluctuations in the ICM can help us to probe the AGN feedback in galaxy clusters (Churazov et al. 2012; Gaspari et al. 2014b; Khatri & Gaspari 2015; Zhuravleva et al. 2016). Effervescent heating is expected to be associated with density fluctuations (in the form of X-ray cavities caused by bubbles), whereas acoustic heating is mainly related to the pressure fluctuations. Accurate measurements of small-scale perturbations are expected from future X-ray satellites such as Athena. This will give us the ability to measure the fluctuations down to a few kpc allowing us to study the relative contribution of AGN feedback models in heating the ICM.

ACKNOWLEDGEMENTS

This work was supported by CNES. AI would like to thank Raman Research Institute, Bangalore and Tata Institute of Fundamental Research, Mumbai for the support during the initial stage of this work. AI would also like to thank Gabriel Pratt and Monique Arnaud for the useful discussions on ICM evolution. SM acknowledges support of the Department of Atomic Energy, Government of India, under project no. 12-R&D-TFR-5.02-0200. We would sincerely like to thank the reviewer, Noam Soker, for his insightful feedback that helped to improve the clarity of this work.

DATA AVAILABILITY

The datasets generated during and/or analyzed in this study are available upon request from the corresponding author.

REFERENCES

Adam R. et al., 2015, A&A, 576, A12
Andrade-Santos F. et al., 2021, ApJ, 914, 58
Arnaud M., Pratt G. W., Piffaretti R., Böhringer H., Croston J. H., Pointecouteau E., 2010, A&A, 517, A92
Babul A., Balogh M. L., Lewis G. F., Poole G. B., 2002, MNRAS, 330, 329
Bandara K., Crampton D., Simard L., 2009, ApJ, 704, 1135
Barnes D. J. et al., 2019, MNRAS, 488, 3003
Battaglia N., Bond J. R., Pfrommer C., Sievers J. L., 2012, ApJ, 758, 74
Begelman M. C., 2001, in Hibbard J. E., Rupen M. P., van Gorkom J. H., eds, ASP Conf. Ser. Vol. 240, Gas and Galaxy Evolution. Astron. Soc. Pac., San Francisco, p. 363
Binney J., Tabor G., 1995, MNRAS, 276, 663
Bîrzan L., Rafferty D. A., Nulsen P. E. J., McNamara B. R., Röttgering H. J. A., Wise M. W., Mittal R., 2012, MNRAS, 427, 3468
Bryan G. L., Norman M. L., 1998, ApJ, 495, 80
Chaudhuri A., Majumdar S., 2011, ApJ, 728, L41
Chaudhuri A., Nath B. B., Majumdar S., 2012, ApJ, 759, 87
CHEX-MATE Collaboration, 2021, A&A, 650, A104
Churazov E., Brüggen M., Kaiser C. R., Böhringer H., Forman W., 2001, ApJ, 554, 261
Churazov E. et al., 2012, MNRAS, 421, 1123
Dubois Y., Devriendt J., Slyz A., Teyssier R., 2010, MNRAS, 409, 985
Dubois Y., Devriendt J., Teyssier R., Slyz A., 2011, MNRAS, 417, 1853
Duffy A. R., Schaye J., Kay S. T., Dalla V. C., 2008, MNRAS, 390, L64
Dunn R. J. H., Fabian A. C., 2006, MNRAS, 373, 959
Fabian A. C., 1994, ARAA, 32, 277
Fabian A. C., Daines S. J., 1991, MNRAS, 252, 17P
Fabian A. C., Reynolds C. S., Taylor G. B., Dunn R. J. H., 2005, MNRAS, 363, 891
Fabjan D., Borgani S., Tornatore L., Saro A., Murante G., Dolag K., 2010, MNRAS, 401, 1670
Gaspari M., Brighenti F., Temi P., Ettori S., 2014a, ApJ, 783, L10
Gaspari M., Churazov E., Nagai D., Lau E. T., Zhuravleva I., 2014b, A&A, 569, 67
Godfrey L. E. H., Shabala S. S., 2013, ApJ, 767, 12
Hillel S., Soker N., 2020, ApJ, 896, 104
Holder G. P., Carlstrom J. E., 2001, ApJ, 558, 515
Iqbal A., Majumdar S., Nath B. B., Ettori S., Eckert D., Malik M. A., 2017a, MNRASL, 465, L99
Iqbal A., Majumdar S., Nath B. B., Ettori S., Eckert D., Malik M. A., 2017b, MNRAS, 472, 713
Iqbal A., Nath B. B., Majumdar S., 2018, MNRASL, 480, L68
Kaiser N., 1986, MNRAS, 222, 323
Kale R., Venturi T., Cassano R., Giacintucci S., Bardelli S., Dallacasa D., Zucca E., 2015, A&A, 581, 23
Khalatyan A., Cattaneo A., Schramm M., Gottlöber S., Steinmetz M., Wisotzki L., 2008, MNRAS, 387, 13
Khatri R., Gaspari M., 2016, MNRAS, 463, 655
Massonneau W., Volonteri M., Dubois Y., Beckmann R. S., 2022, preprint (arXiv:2201.08766)
McCarthy I. G. et al., 2010, MNRAS, 406, 822
McDonald M. et al., 2014, ApJ, 794, 67
Nagai D., Kravtsov A. V., Vikhlinin A., 2007, ApJ, 668, 1
Nath B. B., 2003, MNRASL, 339, 721
Nath B. B., 2004, MNRASL, 353, 941
Nath B. B., Majumdar S., 2011, MNRAS, 416, 271
Nath B. B., Roychowdhury S., 2002, MNRAS, 333, 145
Navarro J. F., Frenk C. S., White S. D. M., 1996, ApJ, 462, 563
Navarro J. F., Frenk C. S., White S. D. M., 1997, ApJ, 490, 493
Okabe N., Takada M., Umetsu K., Futamase T., Smith G. P., 2010, PASJ, 62, 811
Peebles P. J. E., 1980, The Large Scale Structure of the Universe. Princeton Univ. Press, Princeton
Peterson J. R. et al., 2001, A&A, 365, L104
Peterson J. R., Fabian A. C., 2006, Physics Reports, 427, 1
Planck Collaboration V, 2013, A&A, 550, A131
Planelles S. et al., 2017, MNRAS, 467, 3827
Pratt G. W., Croston J. H., Arnaud M., Böhringer H., 2009, A&A, 498, 361
Pratt G. W. et al., 2010, A&A, 511, A85
Puchwein E., Sijacki D., Springel V., 2008, ApJ, 687, L53
Rasera Y., Chandran B., 2008, ApJ, 685, 105
Rasia E. et al., 2015, ApJ, 813, L17
Rephaeli Y., Silk J., 1995, ApJ, 442, 91
Roychowdhury S., Ruszkowski M., Nath B. B., Begelman M. C., 2004, ApJ, 615, 681
Roychowdhury S., Ruszkowski M., Nath B. B., 2005, ApJ, 634, 90
Ruszkowski M., Begelman M. C., 2002, ApJ, 581, 223
Sereno M., Ettori S., 2015, MNRAS, 450, 3675
Shin J., Woo J.-H., Mulchaey J. S., 2016, ApJS, 227, 31
Sijacki D., Springel V., 2006, MNRAS, 366, 397
Soker N., 2022, Universe, 8, 483
Sternberg A., Soker N., 2019, MNRAS, 395, 228
Stott J. P. et al., 2012, MNRAS, 422, 2213
Teyssier R., Moore B., Martizzi D., Dubois Y., Mayer L., 2011, MNRAS, 414, 195
Tozzi P., Norman C., 2001, ApJ, 546, 63
Voigt L. M., Fabian A. C., 2004, MNRAS, 347, 1130
Voit G. M., Kay S. T., Bryan G. L., 2005, MNRAS, 364, 909
Walker S. A., Sanders J. S., Fabian A. C., 2018, MNRAS, 481, 1718
White S. D. M., Rees M. J., 1978, MNRAS, 183, 341
Yang H. -Y. K., Reynolds C. S., 2016, ApJ, 829, 90
Zhuravleva I. et al., 2016, MNRAS, 458, 2902
Zweibel E. G., Mirnov V. V., Ruszkowski M., Reynolds C. S., Yang H.-Y. K., Fabian A. C., 2018, ApJ, 858, 5

This paper has been typeset from a TEX/LATEX file prepared by the author.